FRACTURE OF EUTECTOID STEEL BARS UNDER TENSILE LOADING: EXPERIMENTAL RESULTS AND NUMERICAL SIMULATION

Keywords: Steel, Tensile test, Cohesive zone model, Triaxiality.

Abstract. *Construction steel bars tested under tension usually show a cup-cone fracture pattern. Nevertheless, some steels, such as the eutectoid one used for manufacturing prestressing steel wires, show a different pattern: a flat fracture surface with a dark region inside. This paper presents experimental work performed to identify the fracture mechanisms that trigger this particular flat fracture pattern and numerical simulations where it is reproduced numerically. The experimental tests are carried out on cylindrical specimens of three diameters, 3, 6 and 9mm, subjected to tension. In order to analyse the fracture mechanism, numerical simulations are performed by using the finite element method and the cohesive zone approach. To that end, a cohesive interface element with mechanical properties that depend on the stress triaxiality is presented and assessed. This approach provides reasonably good agreement with the experimental results. In addition, when compared with other popular models such as the GTN model, it presents certain advantages since it requires a smaller number of parameters to be defined.*

1. INTRODUCTION

Steel, together with concrete, is the most widely used material in construction works. Both its high strength and ductility make it especially interesting from the structural safety point of view. This is because under extreme accidental loads it enables stress redistribution with adjacent elements that allows more energy to be dissipated before reaching the structural failure. However, despite being extensively used, there remain certain aspects related to its fracture behaviour that deserve to be clarified and that may allow a better use of its properties in the future.

Because of its simplicity tensile testing is the most extended method for the measurement of the mechanical properties of steels. This method is standardised [1,2] and allows the stress-deformation curve of the material to be obtained. When a steel item is tested under tension and reaches the maximum stress point, a necking process begins and makes it difficult to define the material behaviour from that moment onward. Indeed, because of these difficulties, the last part of the stress-deformation curve that goes from the maximum load point up to fracture is usually neglected when, in the authors' opinion, it contains interesting and valuable information related to structural safety.

The necking process leads to fracture in the thinner section of the necked region and, when testing cylindrical specimens, usually takes place with the typical cup-cone surface pattern, like that shown in Figure 1.

(Figure 1)

The fracture of ductile metals, including construction steels, has usually been explained with the theory of nucleation, growth and coalescence of microvoids. According to this theory, at a first stage and under high stress levels, microvoids are developed inside the material (nucleation) due to a decohesive process of small inclusions that are torn apart from the rest of the material or by the fracture of the particle that constitutes the inclusion itself. At a second stage, and under higher deformational states, these microvoids increase their size (growth) until they become interconnected (coalescence) [3]. Such a process weakens the material until its eventual failure. This theory has formed the basis of several numerical models that have sought to reproduce the fracture on ductile materials, with the Gurson model being the most popular of them [4]. The formulation of this model is based on the behaviour of a spherical void inside an incompressible material under different loading states, studied by Rice and Tracey in 1969 [5]. Since its appearance, Gurson-type models have been applied to various ductile materials, such as aluminium, copper and steel. The subsequent evolution of the Gurson model, proposed by Tvergaard and Needleman, has reproduced not only softening due to the growth of microvoids, but also eventual fracture of the material [6]. In fact, many variations of the Gurson-Tvergaard-Needleman (GTN) model have been proposed since its appearance in 1977, adapting its formulation with additional parameters, such as temperature [7], and correcting its behaviour under different triaxiality states [8, 9, 10].

As previously mentioned, the main advantage of GTN models is that their formulation is based on the physical process that explains the fracture mechanism: nucleation, growth and coalescence of microvoids. Despite its success when modelling the fracture behaviour of many ductile materials, GTN models have two principal disadvantages:

- The first involves the many parameters needed to define the model, which makes it difficult to obtain a valid set of parameters. Furthermore, as Steglich et al. state [11], there is not a single set of valid parameters and different sets can be suitable in reproducing the same experimental result.

- The second involves certain parameters required by the model that cannot be obtained experimentally. For instance, the critical void volume fraction, f_c, is defined as the critical void fraction required for the coalescence process to begin, which cannot be measured by experimental procedures.

These disadvantages do not allow the parameters of the model to be defined *a priori* and lead to a trial-and-error sequence that provides a set of parameters that is able to reproduce experimental results but is not unique.

On another note, although cup-cone fracture is typical of tensile failure in metallic materials with a ductile behaviour, not all construction steels exhibit this fracture pattern. Figure 2 shows the fracture surface of a cylindrical specimen of pearlitic steel, used for manufacturing prestressing steel wires. This type of steel presents a flat fracture surface, perpendicular to the loading direction and with a dark region in the centre of it. Regarding this fracture pattern, the following hypothesis is proposed in this paper: the central dark region is the result of a process of nucleation and growth of microvoids, causing internal damage responsible for the eventual fracture. Therefore, a quasi-brittle fracture takes place as a consequence of a decohesive process, with the dark region acting as a circular crack perpendicular to the loading direction.

(Figure 2)

In order to verify such a hypothesis through numerical simulation, an alternative to GTN models is presented. Based on the previously mentioned hypothesis, a cohesive model is applied to reproduce the failure mechanism on eutectoid steel, used for manufacturing prestressing steel wires. The use of such a cohesive model as a failure mechanism enables an easier calibration, since it requires only two parameters to be defined, f_t and G_F, with the latter being obtainable experimentally. Unlike traditional cohesive crack models [12, 13], that presented here includes the stress triaxiality as a key factor that modifies the cohesive behaviour of the material, since many authors have confirmed in published research that the stress triaxiality state plays an important role in the mechanisms that lead to failure in ductile materials such as steel [14, 15, 16].

Therefore, this paper includes both experimental and numerical results. The experimental work is divided in two sets: the first which checks the validity of the aforementioned hypothesis; and the second which obtains data used for validation of the numerical model proposed. The first set of experimental results includes use of a scanning electron microscope (SEM) to observe the microstructure of the regions that can be identified on the fracture surface of these specimens and an innovative procedure used to observe the internal damage developed inside the specimen before failure. The second set of experimental data includes results of tests carried out with cylindrical specimens of different diameters. Lastly, the decohesive model proposed is presented and the results obtained with it are compared with the experimental data.

2. EXPERIMENTAL WORK

The experimental work carried out in this study consists mainly of tensile tests on cylindrical specimens of three different diameters. Some of these tests are performed until failure as described by the standard [1] and some others are developed by stopping the loading process at the plastic region, submerging the specimens in liquid nitrogen and resuming the tests up to failure in order to induce a brittle fracture in the necking section.

After presenting the material description and the geometrical characteristics of the specimens, the experimental procedure used in the tensile tests is described. The microstructural analysis of the fracture surface is then presented. And lastly, the tensile tests carried out on embrittled specimens are described.

• *Material*

Prestressing steel wires are the result of a manufacturing process in which raw eutectoid steel bars are cold-drawn, reducing their section by pulling them through a conical die. The specimens used in this work are obtained from raw eutectoid steel bars (0.77%C) used for manufacturing prestressing steel wires. This means that as they are not cold-drawn, they can be assumed to behave isotropically. More information on this material can be found in [17] and [18].

The chemical composition of this material can be consulted in Table 1.

(Table 1)

This material, when tested under tension, does not show the typical cup-cone fracture surface, but a flat fracture surface with a dark region in the centre of it (see Figure 2).

• *Specimens*

The specimens are cylindrical and of three diameters: 3, 6 and 9mm. The dimensions of these specimens meet the requirements defined by [19] and are shown in Figure 3.

(Figure 3)

- ***Tensile tests***

Tensile tests are carried out by using a Suzpecar universal testing machine. The test is performed under displacement control at 0.0125 mm/s, 0.02mm/s and 0.03mm/s for the 3, 6 and 9mm diameter specimens respectively. The force is measured with a load cell of 100kN capacity and the strains with an optical extensometry system, registering one image per second. These images are post-processed with the specific software VIC-2D of Correlated Solutions. The resulting load-strain diagrams may be observed in Figure 4.

(Figure 4)

- ***Microstructural analysis of the fracture surface***

The fracture surface of the material analysed in this work shows two clearly defined regions: a dark one in the centre and a light region around it. Different colours on these regions may be the result of distinct fracture mechanisms.

Figure 5 presents the SEM images of the fracture surface of a 9mm diameter specimen, obtained with a JEOL 6400 JSM microscope. As this figure shows, the microstructure corresponding to the central region exhibits the dimples typically related with a nucleation-growth-coalescence mechanism, while the surrounding region shows a morphology that can be attributed to a cleavage mechanism of fracture.

(Figure 5)

This result seems to point towards the hypothesis that fracture takes place in two steps: an initial decohesion mechanism in the centre of the section due to a nucleation-growth-coalescence mechanism and subsequent damage propagation from inside to outside due to a brittle mechanism.

- ***Tensile tests on embrittled specimens***

In order to detect the transition from the nucleation-growth-coalescence mechanism to the cleavage one, additional tensile tests were conducted.

With this aim, two groups of tests are performed on 6mm diameter specimens, with the first one consisting of simple tensile tests carried out until failure for reference and with the second one entailing tensile tests stopped just before failure.

As a result of the first group of tests, the F-[illegible] diagram can be defined with high accuracy. This is necessary for the second group tests to be stopped at desired points of the curve and, subsequently, at different stages of the nucleation-growth-coalescence process inside the specimens.

- *Tests carried out until failure*

As mentioned before, at a first stage specimens are tested in order to obtain the F-ε diagram, which is necessary for the second group of tests. Figure 6 shows the average load-strain (F-ε) curve obtained in these tests.

- *Tests stopped before failure*

Once the F-ε diagram is completely defined, four specimens are tested and stopped at certain points of the diagram after the maximum load point and before failure. Table 2 shows the strain values considered for each of these specimens and Figure 6 shows the position of these points on the F-ε diagram obtained with the initial tests mentioned above.

(Table 2)

(Figure 6)

All the specimens are then tested until failure at an extremely low temperature with an accelerated tensile test; this is performed by submerging the specimens in liquid nitrogen and applying a rapid displacement of the clamping jaws. This procedure produces an embrittled fracture that allows the internal damage to be determined before the accelerated test is carried out without introducing additional damage. During these tests the temperature is measured by using a thermocouple, registering a temperature almost constant during the tests and equal to -100ºC. The experimental setup is shown in Figure 7.

(Figure 7)

- *Results*

None of the fracture surfaces of the specimens tested at the three lower strain levels show any trace of damage after applying the embrittled fracture procedure described above. Nevertheless, the fracture surface of the specimen tested at the highest strain level ($\varepsilon_{12.5}=0.215$) presents a small circular-shaped dark area in the central region of it. Figure 8 shows the fracture surface of this specimen.

(Figure 8)

In addition, this specimen has also been analysed by means of X-ray computed tomography (Nanotom 160NF, Phoenix) before applying the embrittled fracture procedure described above, in order to check the dimension of the internal damage. In principle, X-ray tomography allows the detection of existing internal damage in the specimen, but only when thin specimens are analysed. This test shows internal damage placed at the same exact position as that observed after the embrittled fracture test. Figure 9 compares the result obtained by means of the X-ray tomography technique with the fracture surface after the embrittled test; in this figure the tomographic image has been obtained with a resolution of 2.5 μm per voxel.[1] Both pictures show similar damage at the same position on the cross-section of the specimen. This result confirms that the X-ray tomography technique is also applicable with specimens up to a diameter of, at least, 6mm.

(Figure 9)

3. TRIAXIALITY-DEPENDENT COHESIVE INTERFACE ELEMENT

In this section, the triaxiality-dependent cohesive interface element proposed in this research is presented. While it has been programmed in Fortran for the commercial program ABAQUS, it can be easily adapted to other codes, such as ANSYS and FEAP. The source code of this element can be found in [18].

- *General description of the element behaviour*

The interface element is programmed to reproduce a decohesive process that occurs on the YZ plane, although it could be applied to any other plane. The element is programmed as a quadrilateral interface element, consisting of four coincident pairs of nodes. Four of these nodes are placed on the YZ plane, while their nodal pairs are connected to the brick elements that represent the continuum in which the fracture process is taking place. Figure 10 shows a sketch with the general behaviour of the interface element.

(Figure 10)

Decohesion begins when the X-stress, σ_{xx}, reaches a threshold value equal to the tensile strength, f_t, which, as will later be explained, depends on the stress triaxiality factor, T

$$T = \frac{\sigma_H}{\sigma_{VM}}$$

where σ_H is the spherical part of the stress tensor (volumetric stress) and σ_{VM} the Von Mises equivalent stress.

The element is programmed by using first-order shape functions and the standard isoparametric coordinates for quadrilateral plane elements. The stiffness matrix for each element and its corresponding force vector are calculated by using the Gauss-Legendre integration with four integration points.

- *Large deformations analysis*

As previously mentioned, the stiffness matrix and force vector for each element are integrated by using isoparametric coordinates, which significantly reduces the computational cost of this process

---

[1] This looks fine to me.

[20]. The description of this type of interface elements can be consulted in any publication that examines the finite element method (see, for example, [21], [22] or [23]). In this case it is enough to point out that the real coordinates *(y,z)* and isoparametric coordinates (η, ξ) can be related by means of the Jacobian matrix J_e.

The determinant of J_e allows the differential area in both coordinate systems to be expressed as follows:

$$d A_e = dydz = \left| J_e \right| d\eta d\xi$$

Therefore, when using the isoparametric coordinates, the stiffness matrix of an element can be integrated by using the expression (1).

$$K_e = \int_{-1}^{1} \int_{-1}^{1} B_e^T D B_e t \left| J_e \right| d\eta d\xi \qquad (1)$$

where $\boldsymbol{B_e}$ represents the strain-displacement matrix and $\boldsymbol{D}$ the stress-strain matrix.

When modelling materials such as steel, which develops large deformations before failure, the area of the interface element is reduced as the deformation process takes place. Figure 11 shows the result of this effect.

(Figure 11)

In order to consider the effect of large deformations, in the cohesive interface element presented here the value of $\left| J_e \right|$ is updated after every time increment given during the non-linear calculation process. To this end, the nodal coordinates are updated after every time increment and $\left| J_e \right|$ is recalculated for the next increment.

- ***The role of the stress triaxiality state***

As mentioned in the introduction, the stress triaxiality state has been shown as a key factor in the fracture behaviour of ductile materials. This is the reason why the cohesive behaviour of the interface element presented in this paper has been defined as dependent on the stress triaxiality (σ_{H}/σ_{VM}). This is done by using a multiplicative factor, *F*, which is a function of the stress triaxiality factor *T* and affects the cohesive behaviour of the element by modifying the tensile strength f_t and the fracture energy G_F, which define the softening curve of the material.

Since the interface element is bidimensional and unable to provide the triaxiality state itself, the stress triaxiality factor is obtained with the brick element connected to it.

In order to obtain the stress triaxiality factor of an interface, the stress tensor of the brick element connected to it is stored at every time increment along the calculation process. This stress tensor is used in the next time increment to obtain the Von Mises stress, the hydrostatic stress and, therefore, the stress triaxiality factor. This factor allows the factor F, which is used to update the softening curve parameters f_t and G_F, to be obtained.

$$\begin{cases} f_t^{¿}=f_t \times F \\ G_F^{¿}=G_F \times F \end{cases}$$

Hence, to obtain the stress triaxiality factor of a certain time increment, the previous time increment tensor is used, since ABAQUS does not allow the values within the current increment to be used. This was also observed by Scheider [24], who showed that the error induced by it does not provide a significant deviation, since the time increment is always small in order to achieve numerical convergence.

Figure 12 shows how this process is carried out with the interface element presented here.

(Figure 12)

4. NUMERICAL SIMULATION

The specimens of the three diameters (3, 6 and 9mm) tested are reproduced numerically by using the interface cohesive element described in the previous section. The experimental predictions are compared with the numerical results in order to validate the model presented in this paper.

• *Geometry and boundary conditions*

Taking benefit from the axial symmetry of the problem, only 1/24th of each specimen is modelled, as shown in Figure 13. The load is applied in the direction of the X axis and the YZ plane corresponds to the fracture plane.

(Figure 13)

The boundary conditions can be described as follows:

- Nodes on the XZ plane (plane 1): displacements in the XZ plane are permitted while displacements in the direction of the Y axis are not.
- Nodes on the plane inclined at 30º with respect to XZ plane (plane 2): displacements on this inclined plane are permitted, while displacements perpendicular to it are not.

No additional boundary conditions are needed. The nodes placed in the YZ plane (plane 3) are implicitly constrained by the cohesive behaviour of the interface elements, as mentioned before, to which they are connected. Given that these nodes are not constrained on the YZ plane, the fracture energy released by the decohesion process is only due to a mode I case, which agrees with the experimental estimate of the fracture energy G_F.

- ***Loading***

Load is applied by prescribing a defined displacement on the end of the specimen placed at the opposite end of the decohesion plane (plane 4).

- ***Materials***

Two materials are defined: one for the brick elements of the continuum that are out of the fracture plane and another for the fracture plane. For the brick elements of the continuum an elastoplastic material is defined. Such elastoplastic behaviour is defined by means of the $\sigma - \varepsilon_{p}$ curve of the material.

The material for the fracture plane is modelled by using the cohesive interface elements described before. The parabolic softening function shown in Figure 14 is considered. The reason for this is that, although a rectangular softening function is convenient when dealing with metals [25], it has many convergence issues when implemented in a numerical model. These convergence issues can be avoided by using the parabolic function proposed here. Only two parameters are needed to define this function, the fracture energy G_F and the decohesion stress f_t. The first of them is obtained experimentally by means of standardised three-point bending tests according to the [26] and the second one is estimated to match the experimental results. The results of these parameters used in the simulations are presented in the Table 3.

(Figure 14)

(Table 3)

As mentioned before, the cohesive behaviour of the interface elements depends on the stress triaxiality. This is done by defining a factor F, dependent on the stress triaxiality factor (T), which is expressed in (2). According to this expression, the higher the value of T, the higher the value of F and, therefore, the values of f_t and G_F increase when the material is subjected to higher values of T. It should be noted that such a relationship and its deduction is beyond the scope of this study. For further information, the reader is addressed to [27].

$$\begin{cases} F=1 & if \quad T\le\frac{1}{3} \\ F=1+\left(\frac{T-\frac{1}{3}}{80}\right)^{\frac{1}{3}} & if \quad \frac{1}{3}<T<\frac{2}{3} \\ F=1+\left(\frac{1}{240}\right)^{\frac{1}{3}} & if \quad \frac{2}{3}\le T \end{cases} \tag{2}$$

- ***Simulation of the fracture process***

When a bar of a metallic material is subjected to tension, the plastic strains that develop once the material exceeds the yield limit lead to a concentrated stretching of the material at a certain section of the specimen usually referred to as necking. Such necking induces a stress concentration in the centre of the eventual fracture plane and gives rise to an increase of the stress triaxiality factor *T*. The increment of *T* is accompanied by an increase of the factor *F* and thus affects the value of f_t; therefore, a competition between the stress localisation and the increase of f_t takes place until the normal stress equals the updated value of f_t. The decohesion process begins once the interface element placed at the centre of the specimen reaches a value of σ_{xx} equal to f_t. This decohesive process unloads the brick element adjacent to the interface element and increases the stress at the elements around it. Therefore, the fracture process propagates from inside to outside.

The pictures in Figure 15 show how the decohesion process propagates in the numerical simulation. It should be noted that the strains in the displacements of the nodes on the X axis have been magnified by a factor of 100 in order to make them more noticeable.

(Figure 15)

5. RESULTS

The results obtained experimentally for each of the three specimen diameters are compared with those obtained with the numerical model proposed in this paper. In order to assess the influence of the gradient of strains that takes place in the necking region, three initial gauge lengths are used:

- Fixed gauge length: L=12.5mm
- Gauge length proportional to the specimen diameter: L= 1 ㄹㅂ
- Gauge length proportional to the specimen diameter: L= 2 ㄹㅂ

Figure 16 shows these lengths for each of the diameters considered.

(Figure 16)

Figures 17, 18 and 19 show the results obtained for each of these gauge lengths. The F-ㄹㅁ graphs obtained numerically (red filled lines) are overlaid on those obtained experimentally (black dotted lines). In the case of the numerical results, a white triangle shows the onset of the decohesive process and a white square marks the instant of failure, which has been considered to take place when the decohesive circular area reaches a diameter equal to the dark area measured experimentally, after which the load decreases considerably to a point where the computation became unstable.

(Figure 17)

(Figure 18)

(Figure 19)

Tables 4, 5 and 6 show the ultimate strain values (ε_{ult}) and the difference between the ultimate strain value and the strain at maximum loading $\varepsilon_{ult} - \varepsilon_{\sigma_{max}}$ obtained for each diameter, both numerically (red filled circles and triangles) and experimentally (black empty circles and triangles). These results are plotted in Figures 20, 21 and 22.

(Table 4)

(Table 5)

(Table 6)

(Figure 20)

(Figure 21)

(Figure 22)

It should be noted that these results were obtained with the same material parameters for each model. The curves presented in Figures 17, 18 and 19 were not adjusted individually, but obtained with the same material parameters initially defined.

- ***Comments***

Results corresponding to the fixed gauge length equal to 12.5mm and the numerical simulations seem to predict the experimental results reasonably well (see Figure 17). Nevertheless, while in the specimens of 3 and 9mm diameter the numerical results remain within the experimental limit values, the 6mm diameter numerical result is smaller than all the experimental values (see Figure 20). It is interesting to observe how in the numerical models the decohesive process starts at the last moment of the test and close to the ultimate strain value (Figure 17), also in good agreement with the experimental evidences.

In the case of the proportional gauge length equal to 1 ㄹㅂ, the numerical results of the 3 and 9mm diameter specimens remain in the experimental limit values, while that of the 6mm diameter specimen is smaller than the experimental results (see Figure 21). Once again the decohesive process starts close to the ultimate strain value (Figure 18). In that of the proportional gauge length equal to 2 ㄼ, the 6mm and 9mm numerical results agree quite well with those obtained experimentally (see Figure 22). In the case of the 6 and 9mm specimens, the numerical values are slightly smaller than the experimental ones. Again, the decohesive process always begins close to the ultimate strain value (Figure 19).

If the $\varepsilon_{ult}-\varepsilon_{\sigma_{max}}$ value is analysed, the influence of the specimen thickness on the strain measurement can be observed. It is generally accepted that the maximum load point identifies the beginning of the necking process and the strain at which this takes place is approximately equal in all specimens for all three gauge lengths. Nevertheless, the strain developed between the beginning of necking and failure ($\varepsilon_{ult}-\varepsilon_{\sigma_{max}}$ ¿ increases with the diameter when the fixed gauge length of 12.5mm is used (see Figure 20), though it is quite constant for the two proportional gauge lengths, 1 ㄼ and 2 ㄼ (see Figures 21 and 22). Figure 23 shows the necking region in a specimen of each of the three considered diameters; white lines identify the 12.5mm gauge length.

(Figure 23)

Therefore, proportional gauge lengths 1 ㄼ and 2 ㄼ measure the strain considering proportional regions of the specimen, whereas the 12.5 gauge length measures regions that are not comparable between different diameters. As can be seen in Figure 23, the 12.5 gauge length captures the whole necking region in the 3mm-diameter specimen plus an additional length unaffected by necking. In the case of the 6mm-diameter specimen, it captures the necking region plus a short additional extension of the specimen unaffected by necking and in the case of the 9-mm diameter specimen it barely covers the necking region. For instance, the value of ε_{ult} in the 3mm-diameter specimen measures the strain at a region that includes the necking zone and also part of the specimen unloaded when necking starts. Therefore, it cannot be compared with the results of the 6 and 9-mm diameter specimens.

Finally, Figures 21 and 22 show that $\varepsilon_{ult}-\varepsilon_{\sigma_{max}}$ tends to decrease slightly in the numerical models for both proportional gauge lengths. This because the size of the dark region observed on the specimen fracture surface is not proportional to the specimen diameter. This then gives rise to the hypothesis formulated in the introduction that states that the dark region is the result of the nucleation and coalescence of microvoids process, which has been modelled with the cohesive behaviour of the interface element.

- ***Discussion***

The results described above show that the interface element proposed in this paper can be used to model the tensile failure of this type of materials, especially regarding the fixed gauge length of 12.5mm and a proportional gauge length of 2 ㄼ. It should be noted that since the necking process induces a concentrated gradient of strains around the fracture plane, the strain becomes higher as it nears the centre of the necking. Therefore, it would seem that those results obtained with a small gauge length are more sensitive and present a higher variability.

From the phenomenological point of view, the numerical model reproduces the same process observed experimentally, which is local damage that evolves in the centre of the smallest section of the necking region and spreads from inside to outside.

As a result, the model proposed can be used as a good alternative to the GTN model, since it provides a failure criteria that needs a small amount of parameters to be defined, some of which can be estimated by means of standardised tests. This is especially interesting when compared with the GTN models, which provide good results but require a large amount of parameters to define and are not easily measured experimentally. Nevertheless, some issues should be addressed to make this model more effective, since there is no standardised method available to define the decohesion stress f_t and the stress triaxiality dependence remains unclear.

Nevertheless, this model does not explain the transition from a ductile fracture to a brittle fracture mechanism which is responsible for the visible dark regions observed in the fracture surfaces of the specimens. The brittle fracture seems to compete with the ductile fracture up to an instant when the former is predominant. Given that the model used here only deals with the ductile fracture mechanism, further research is needed to identify the parameters that govern the ductile-brittle transition.

6. CONCLUSIONS

This paper presents the results of experimental and numerical works on the study of the fracture mechanism under tensile loading of cylindrical specimens obtained from raw eutectoid steel bars (0.77%C) used for manufacturing prestressing steel wires.

On the experimental side, several techniques have been used to analyse and localise the onset of the fracture mechanism that takes place. The SEM analysis allows identification of two regions when a fracture surface of one specimen is observed after testing. These results confirm that the eventual failure is the result of a decohesive process that takes place in the centre of the fracture plane and which, once it reaches a certain diameter, triggers a brittle fracture along the plane perpendicular to the loading direction.

The tests carried out on specimens partially tested at a first state, and then tested after being submerged in liquid nitrogen to provoke a brittle fracture, have permitted the point at which the onset of the decohesive process takes place to be identified. This occurs at a strain value close to the ultimate strain.

On the numerical side, a cohesive interface element affected by stress triaxiality has been proposed. By using always the same material parameters, this interface element allows reproduction of the tensile tests carried out experimentally on three diameters and using three initial gauge lengths. This type of model requires only two initial values to be defined: the fracture energy G_f and the decohesion stress f_t, with the first being experimentally obtainable by standard tests [25,28].

The numerical models performed by using this cohesive interface element reproduce a fracture process that is phenomenologically similar to that observed experimentally: a decohesive process takes place in the centre of the smallest section in the necking region and develops from inside to outside. Similar to the experimental observations, this process takes place in the last part of the test when the strain is close to the ultimate strain value.

ACKNOWLEDGEMENTS

The authors gratefully acknowledge the financial support provided for this research by the Spanish Ministerio de Economía y Competitividad under grant DPI 2011-24876.

They also express their gratitude to Federico Sket and Jon M. Molina-Aldareguia, from IMDEA Materiales, for their support with the X-ray computerised tomographic system.

Fernando Suárez wishes to express his gratitude to the Fundación Agustín de Betancourt for the grant provided.

REFERENCES

[1] ISO 15630-1. Steel for the reinforcement and prestressing of concrete – Test methods – Part 1: Reinforcing bars, wire rod and wire, (2010).

[2] ASTM E8 / E8M-13a Standard Test Methods for Tension Testing of Metallic Materials, *ASTM International, West Conshohocken, PA* (2013).

[3] Anderson, T.L.: Fracture mechanics: Fundamentals and applications, *CRC Press.* (1995)

[4] Gurson, A.L.: Continuum Theory of Ductile Rupture by Void Nucleation and Growth: Part I – Yield Criteria and Flow Rules for Porous Ductile Media, *J. Eng. Mater. Tech.* (1977)

[5] Rice, J.R., Tracey, D.M., On the ductile enlargement of voids in triaxial stress fields. *Journal of the Mechanics and Physics of Solids*, vol. 17, nº3, pp 201-217 (1969)

[6] Tvergaard, V., Needleman, A., Analysis of the cup-cone fracture in a round tensile bar, *Acta metall.* Vol. 32, No. 1, pp. 157-169 (1984).

[7] Hao S., Brocks W., The Gurson-Tvergaard-Needleman model for rate and temperature-dependent materials with isotropic and kinematic hardening. Computational Mechanics, Vol. 20, pages 34-40, (1997).

[8] Nahshon K., Hutchinson J.W., Modification of the Gurson Model for shear failure, European Journal of Mechanics – A/Solids, vol. 27, no. 1, pages 1-17, (2008).

[9] Nielsen K. L., Tvergaard V., Effect of a shear modified Gurson model on damage development in a FSW tensile specimen. International Journal of Solids and Structures, Vol. 46, pages 587-601, (2009).

[10] Jackiewicz J., Use of a modified Gurson model approach for the simulation of ductile fracture by growth and coalescence of microvoids under low, medium and high stress triaxiality loadings. Engineering Fracture Mechanics, Vol. 78, no. 3, pages 487-502, (2011).

[11] Steglich D., Siegmund T., Brocks W., Micromechanical modeling of damage due to particle cracking in reinforced metals. Computational Materials Science, Vol. 16, pages 404-413, (1999).

[12] Hillerborg A., Modéer M., Petersson P. E., Analysis of crack formation and crack growth in concrete by means of fracture mechanics and finite elements. Cement and Concrete Research, Vol. 6, no. 6, pages 773-781, (1976).

[13] Bazant Z.P., Planas J., Fracture and size effect in concrete and other quasibrittle materials. New Directions in Civil Engineering. Taylor & Francis, (1997).

[14] Mirza M.S., Barton D.C., Church P., Sturges J.L., Ductile Fracture of Pure Copper: An Experimental and Numerical Study. J. Phys. IV France, Vol. 07, pages C3-891 – C3-896, (1997).

[15] Bao Y., Prediction of ductile crack formation in uncracked bodies. PhD thesis, Massachusetts Institute of Technology, (2003).

[16] Bao Y., Wierzbicki T., On fracture locus in the equivalent strain and stress triaxiality space. International Journal of Mechanical Sciences, Vol. 46, no. 1, pages 81-98 (2004).

[17] Atienza J. M., Tensiones residuales en alambres de acero trefilados, PhD thesis, Universidad Politécnica de Madrid, (2001).

[18] Suárez F., Estudio de la rotura en barras de acero. Aspectos experimentales y numéricos, PhD thesis, Universidad Politécnica de Madrid (2013).

[19] UNE-EN ISO 6892-I. Materiales metálicos. Ensayos de tracción. Parte 1: Método de ensayo a temperature ambiente, (2010).

[20] Irons, B. M. and O. C. Zienkiewicz, The Isoparametric Finite Element System – A New Concept in Finite Element Analysis, *Proc. Conf. Recent Advances in Stress Analysis*. Royal Aeronautical Society. London (1968).

[21] Zienkiewicz O. C., Taylor R. L., Finite Element Method (2000).

[22] Hughes T.J.R., The Finite Element Method: Linear Static and Dynamic Finite Element Analysis, Dover Civil and Mechanical Engineering (1987).

[23] Logan D.L., A First Course in the Finite Element Method, Fourth Edition, Thomson (2007).

[24] Scheider, I., Derivation of separation laws for cohesive models in the course of ductile fracture. *Engineering Fracture Mechanics*,vol. 76, no. 10, pages 1450 – 1459 (2009).

[25] Dugdale D.S., Yielding of steel sheets containing slits, *Journal of the Mechanics and Physics of Solids*. Vol. 8, no. 2, pp.100-104 (1960).

[26] ASTM E 399 – 90. Standard Test Method for Linear-Elastic Plane-Strain Fracture Toughness KIc of Metallic Materials, ASTM International,West Conshohocken, PA (2012)

[27] Siegmund T., Brocks W., A numerical study on the correlation between the work of separation and the dissipation rate in ductile fracture, *Eng. Fract. Mech*. 67, pp.139-154 (2000).

[28] ASTM E 1820 – 13. Standard Test Method for Measurement of Fracture Toughness, ASTM International,West Conshohocken, PA (2013).

TABLES

Table 1

Chemical composition of the eutectoid steel used in this study

C (%)	Si (%)	Mn (%)	P (%)	S (%)	Cr (%)	Mo (%)	Ni (%)	Cu (%)	Al (%)	Ti (%)	Nb (%)	V (%)	N (%)
0.83	0.25	0.72	0.012	0.004	0.24	<0.01	0.02	0.01	<0.003	<0.005	<0.005	<0.01	0.0097

Table 2

Strain rate of each of the four specimens tested under embrittled fracture. A gauge length of 12.5mm is considered.

Specimen	**[illegible] 12.5**
1	0.155
2	0.180
3	0.205
4	0.215

Table 3

Fracture parameters used for the parabolic softening function

f_t [MPa]	G_F [MPa·m]
1450	$8.0 \cdot 10^{-3}$

Table 4

ε_{ult} and $\varepsilon_{\sigma_{max}}$ obtained for each of the three specimen diameters by using a fixed initial gauge length equal to 12.5mm.

	Experimental results		**Numerical results**	
	ε_{ult}	$\varepsilon_{\sigma_{max}}$	ε_{ult}	$\varepsilon_{\sigma_{max}}$
ㄹㅂ=3mm	0.1600	0.0743	0.1279	0.0702
	0.1466	0.0761		
	0.1330	0.0709		
ㄹㅂ=6mm	0.1946	0.0831	0.1758	0.0711
	0.2346	0.0789		
	0.2144	0.0772		
ㄹㅂ=9mm	0.2505	0.0755	0.2277	0.0804
	0.2132	0.0700		
	0.2237	0.0849		

Table 5

ε_{ult} and $\varepsilon_{\sigma_{max}}$ obtained for each of the three specimen diameters by using a proportional initial gauge length equal to 1 ㄹㅂ

	Experimental results		Numerical results	
	ε_{ult}	$\varepsilon_{\sigma_{max}}$	ε_{ult}	$\varepsilon_{\sigma_{max}}$
	-	-		
ㄹㅂ=3mm	0.2962	0.0852	0.2979	0.0861
	0.2784	0.0733		
	0.2863	0.0864		
ㄹㅂ=6mm	0.3288	0.0780	0.2768	0.0847
	0.3081	0.0770		
	0.2894	0.0756		
ㄹㅂ=9mm	0.2485	0.0722	0.2697	0.0842
	0.2607	0.0939		

Table 6

ε_{ult} and $\varepsilon_{\sigma_{max}}$ obtained for each of the three specimen diameters by using a proportional initial gauge length equal to 2 ㄼ

	Experimental results		Numerical results	
	ε_{ult}	$\varepsilon_{\sigma_{max}}$	ε_{ult}	$\varepsilon_{\sigma_{max}}$
ㄼ=3mm	-	-	0.2021	0.0797
	0.2065	0.0813		
	0.2010	0.0763		
ㄼ=6mm	0.1984	0.0824	0.1813	0.0723
	0.2386	0.0779		
	0.2175	0.0771		
ㄼ=9mm	0.2031	0.0717	0.1778	0.0752
	0.1817	0.0700		
	0.1927	0.0878		

FIGURES

FIGURE CAPTIONS

Figure 1: Cup-cone fracture surface pattern

Figure 2: Flat fracture surface pattern observed on the specimens tested in this study

Figure 3: Principal dimensions of the specimens

Figure 4: Load-strain curves obtained experimentally for each of the three diameters considered by using an initial gauge length of 12.5mm

Figure 5: SEM analysis on the fracture surface of a 9mm diameter specimen. The white dotted circle represents the dark region observed after tensile testing: a) Detail of the microstructure out of the dark region; b) Detail of the microstructure inside the dark region.

Figure 6: F ㅅㅅ ㄹㅁ diagram for a 6mm diameter specimen. Circles identify the maximum strain reached for each of the specimens before the embrittled material tests.

Figure 7: Experimental setup for the embrittled material test. The specimen is submerged in liquid nitrogen by using a plastic recipient and the temperature is measured by means of a thermocouple.

Figure 8: Fracture surface after the embrittled material test corresponding to the specimen initially tested up to the highest strain rate (ㄹㅁ$_{12.5}$=0.215). A dark region can be identified.

Figure 9: Internal damage observed in the specimen initially tested up to the highest strain rate(ㄹㅁ$_{12.5}$=0.215). Fracture surface after the embrittled material test on the left and the X-ray tomography obtained before the embrittled material test on the right.

Figure 10: Behaviour of the interface element. The forces are applied along the X axis and the interface element is contained in the YZ plane.

Figure 11: Large strains lead to a reduction of the cross-sectional area of the brick element and, therefore, to a change of shape of the interface element.

Figure 12: Influence of the stress triaxiality on the softening curve parameters f_t and G_F

Figure 13: Grid used to simulate the experimental tensile tests carried out on the 6mm diameter specimens.

Figure 14: Parabolic softening curve corresponding to a fracture energy G_F=10N·mm/mm^2 and a tensile strength f_t=1525MPa.

Figure 15: Damage evolution on the numerical model (Note: deformation along the X axis is magnified by a factor equal to 100): a) Before loading; b) Stress concentration in the centre of the cross

section; c) Decohesive process begins in the centre of the cross section; d) Decohesive process propagates from inside to outside.

Figure 16: Models dimensions: a) 3mm diameter specimens; b) 6mm diameter specimens; c) 9mm diameter specimens.

Figure 17: Load-strain curves obtained experimentally and numerically for each of the three diameters considered using an initial gauge length of 12.5mm.

Figure 18: Load-strain curves obtained experimentally and numerically for each of the three diameters considered using a proportional initial gauge length of 1 ㄹㅂ ㄱㅅ

Figure 19: Load-strain curves obtained experimentally and numerically for each of the three diameters considered using a proportional initial gauge length of 2 ㄹㅂ ㄱㅅ

Figure 20: ε_{ult} and $\varepsilon_{ult}-\varepsilon_{\sigma_{max}}$ obtained for each of the three specimen diameters using a fixed initial gauge length equal to 12.5mm.

Figure 21: ε_{ult} and $\varepsilon_{ult}-\varepsilon_{\sigma_{max}}$ obtained for each of the three specimen diameters using a proportional initial gauge length equal to 1 ㄹㅂ.

Figure 22: ε_{ult} and $\varepsilon_{ult}-\varepsilon_{\sigma_{max}}$ obtained for each of the three specimen diameters using a proportional initial gauge length equal to 2 ㄹㅂ.

Figure 23: Necking region before failure in specimens of the three considered diameters: 3, 6 and 9mm. The white lines represent the fixed gauge length of 12.5mm.

FIGURE 1

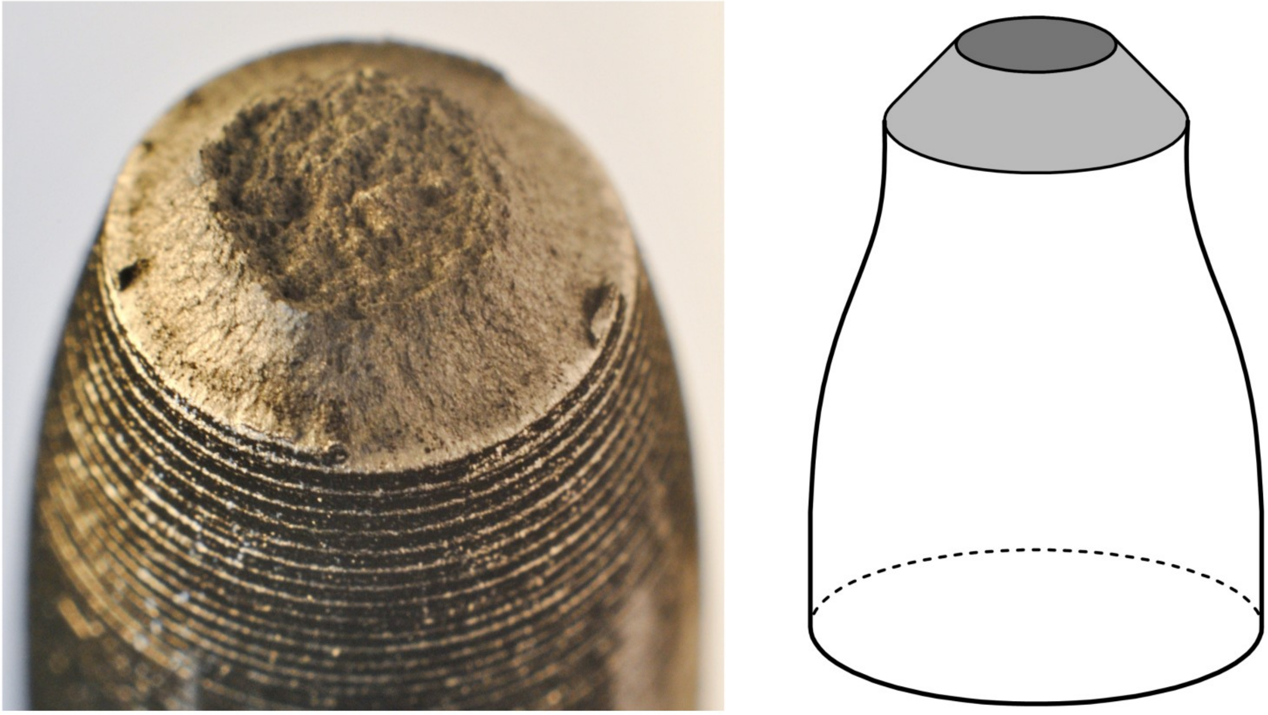

FIGURE 2

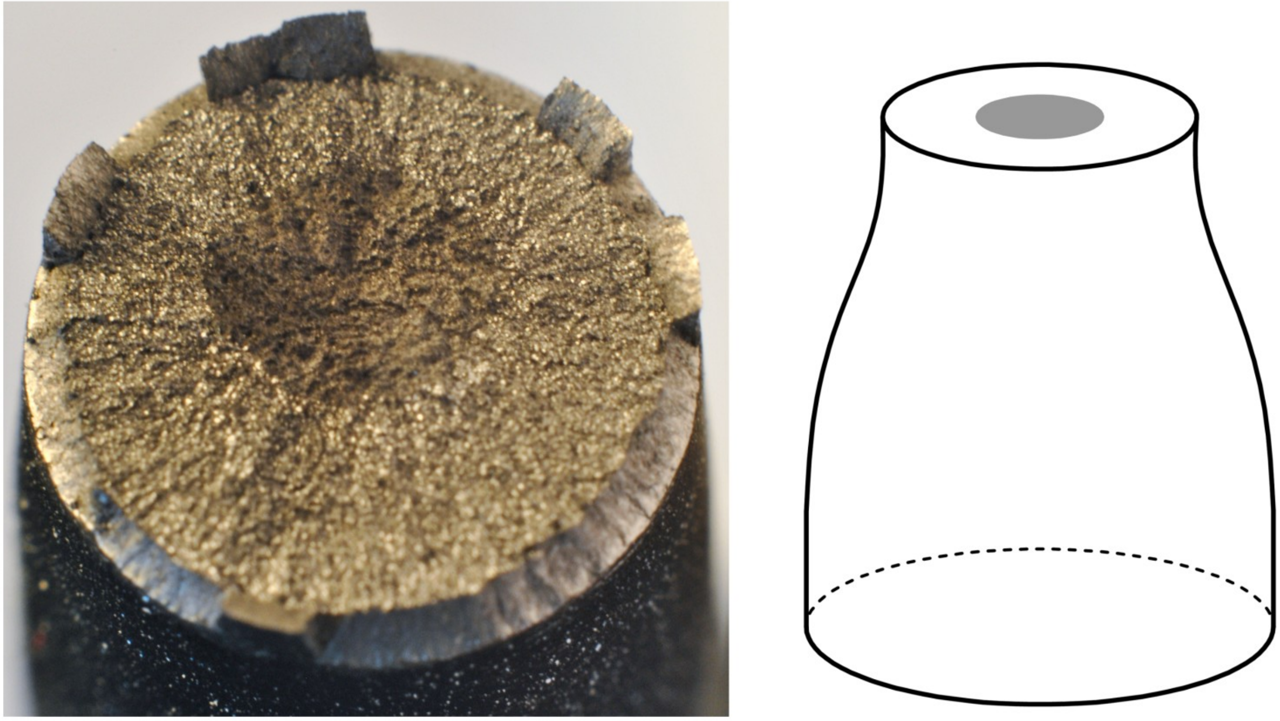

FIGURE 3

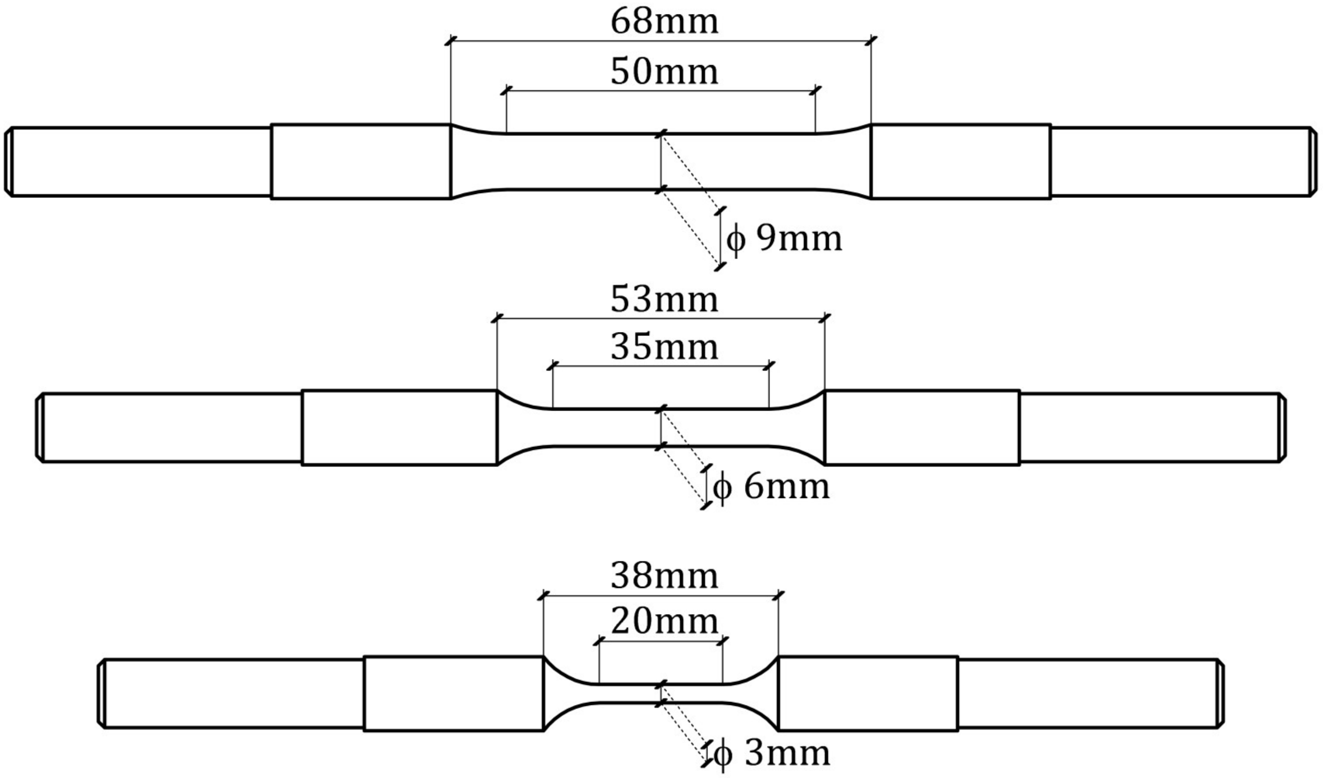

FIGURE 4

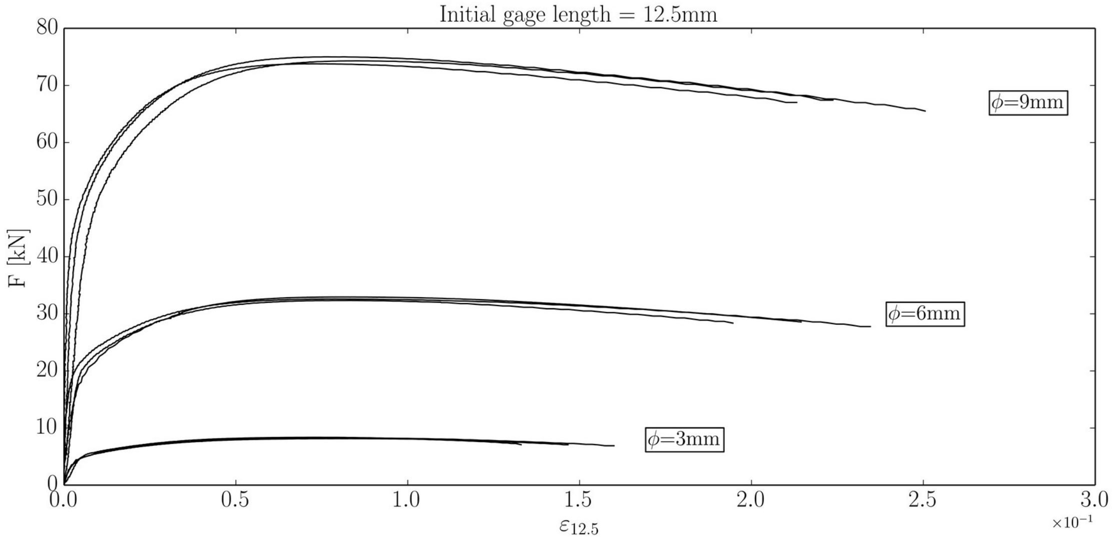
Initial gage length = 12.5mm
F [kN]
$\varepsilon_{12.5}$
$\times 10^{-1}$
0
10
20
30
40
50
60
70
80
0.0
0.5
1.0
1.5
2.0
2.5
3.0
ϕ=9mm
ϕ=6mm
ϕ=3mm

FIGURE 5

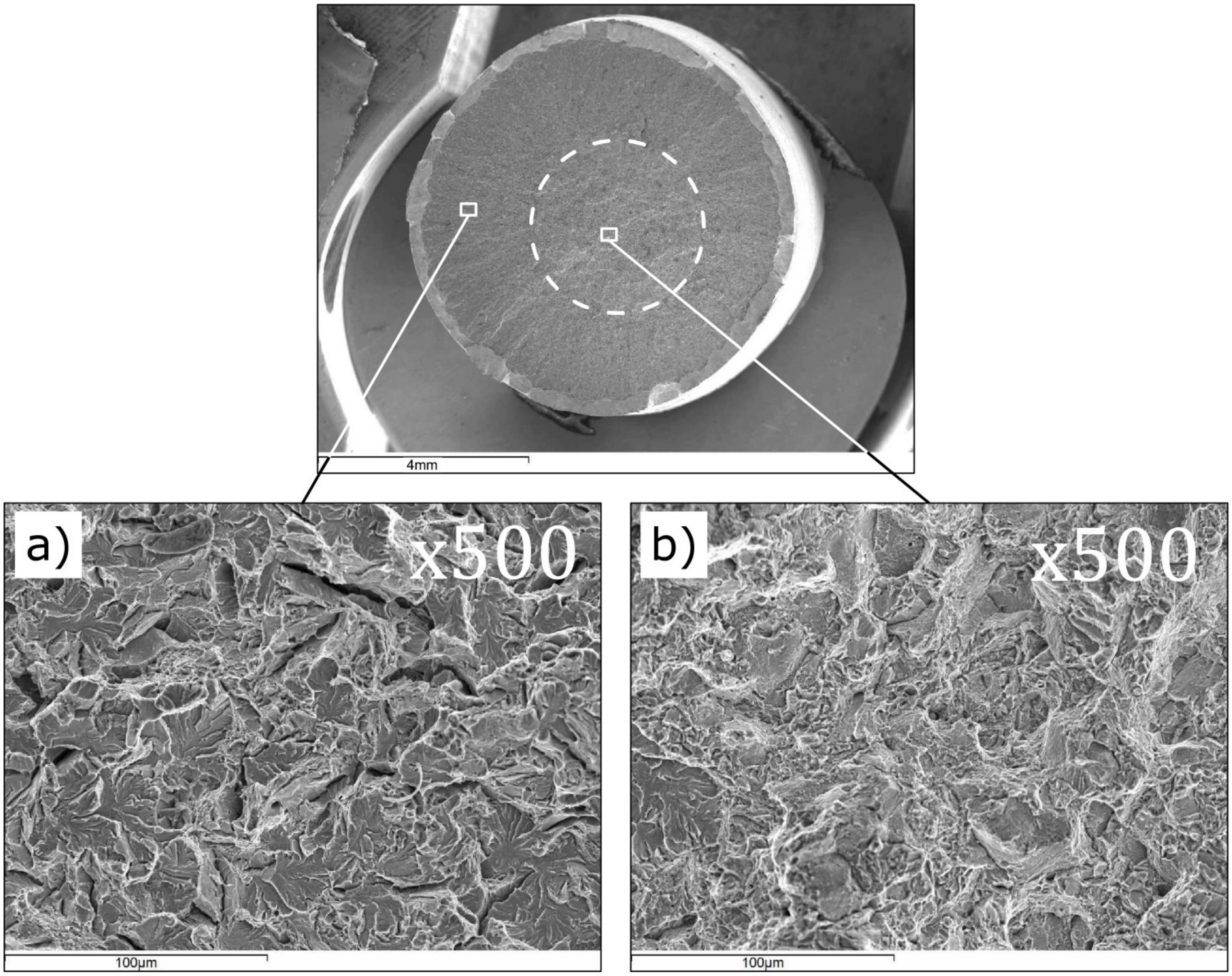

FIGURE 6

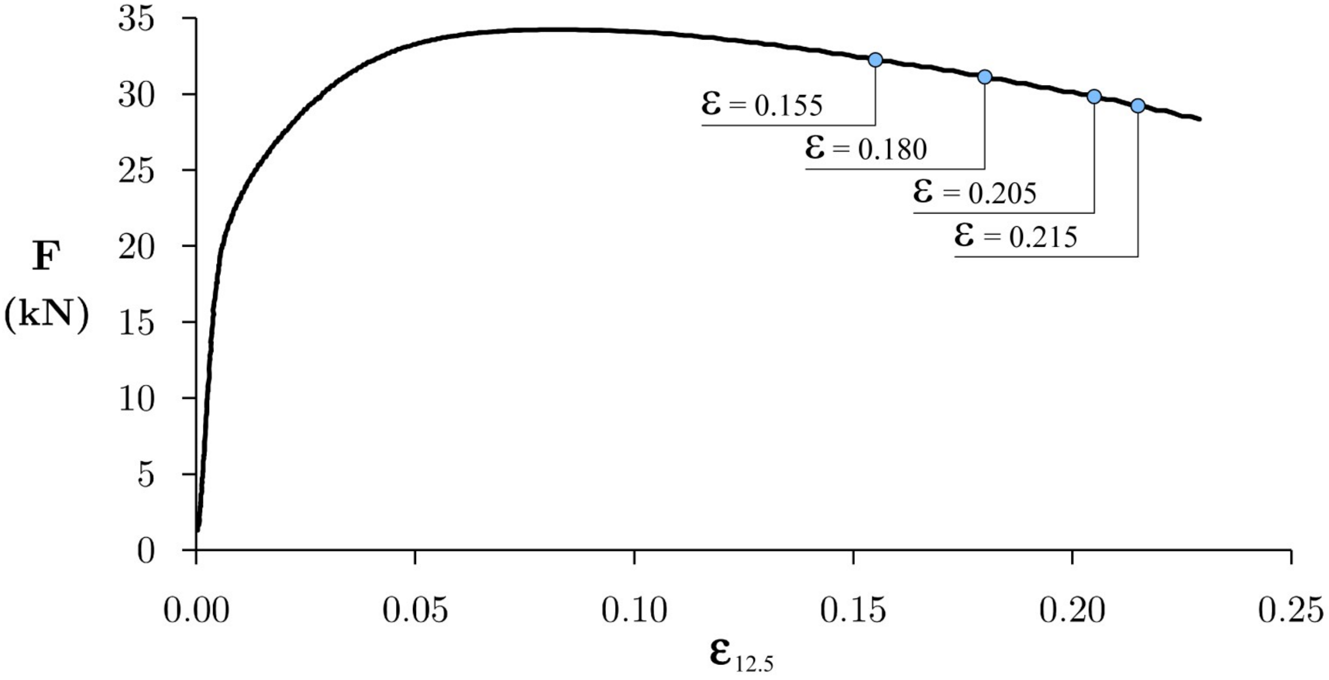
F
(kN)
35
30
25
20
15
10
5
0
0.00
0.05
0.10
0.15
0.20
0.25
$\varepsilon_{12.5}$
ε = 0.155
ε = 0.180
ε = 0.205
ε = 0.215

FIGURE 7

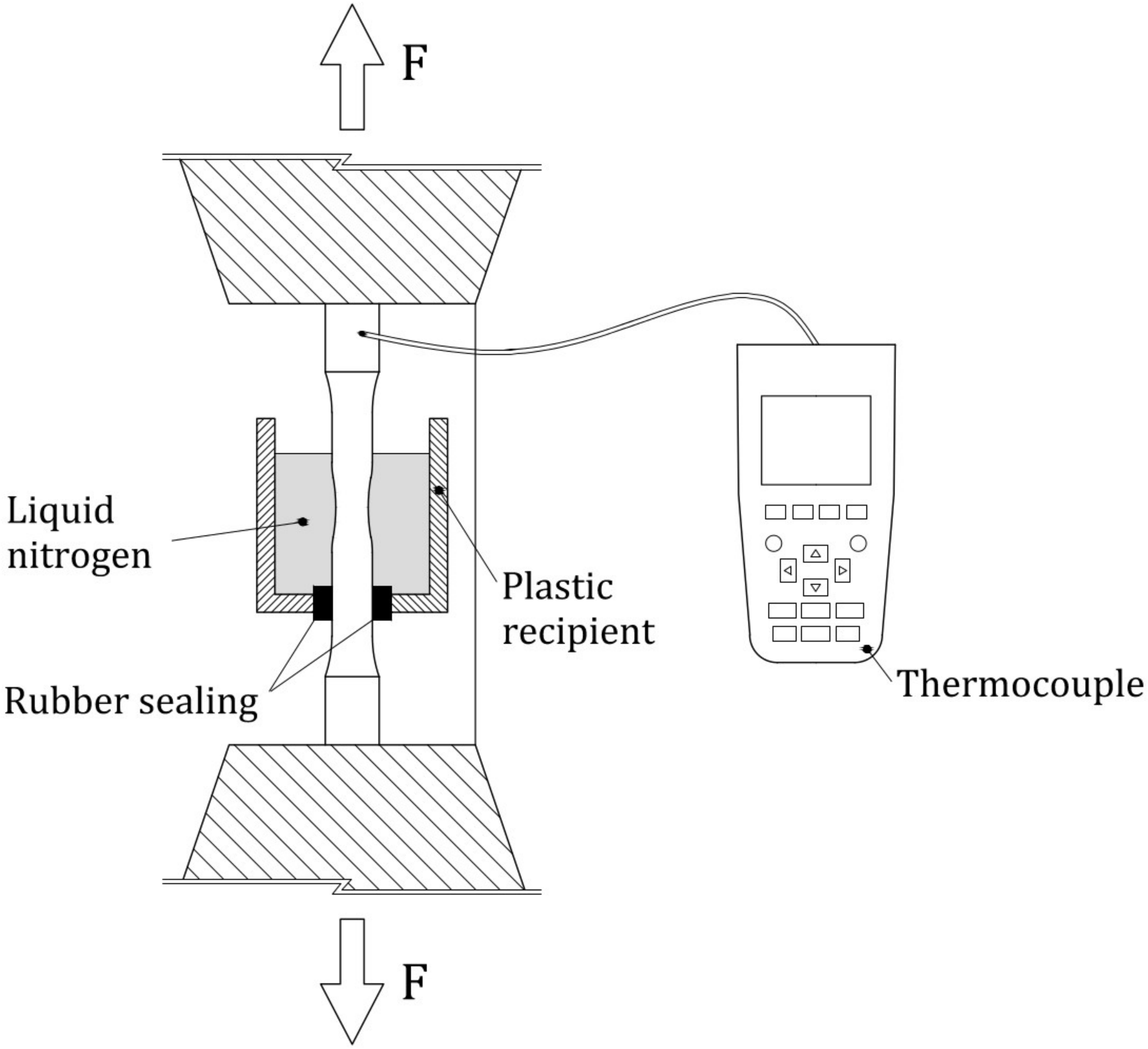
F
Liquid nitrogen
Plastic recipient
Rubber sealing
Thermocouple
F

FIGURE 8

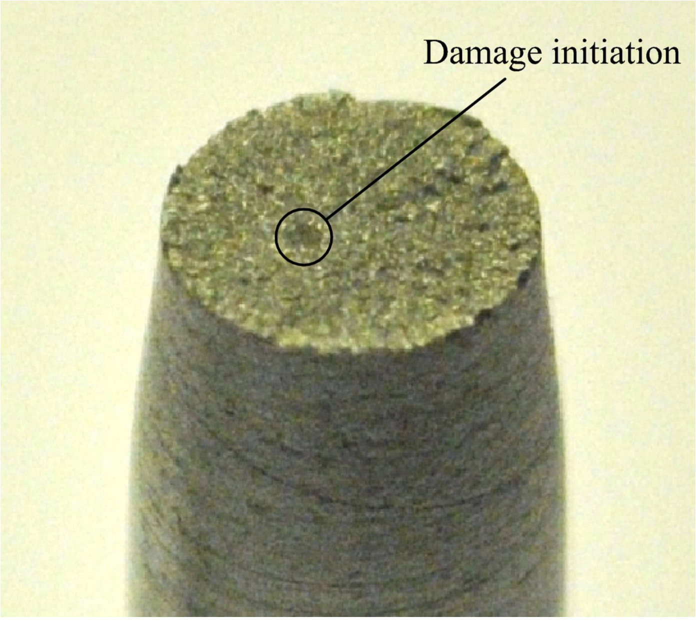

FIGURE 9

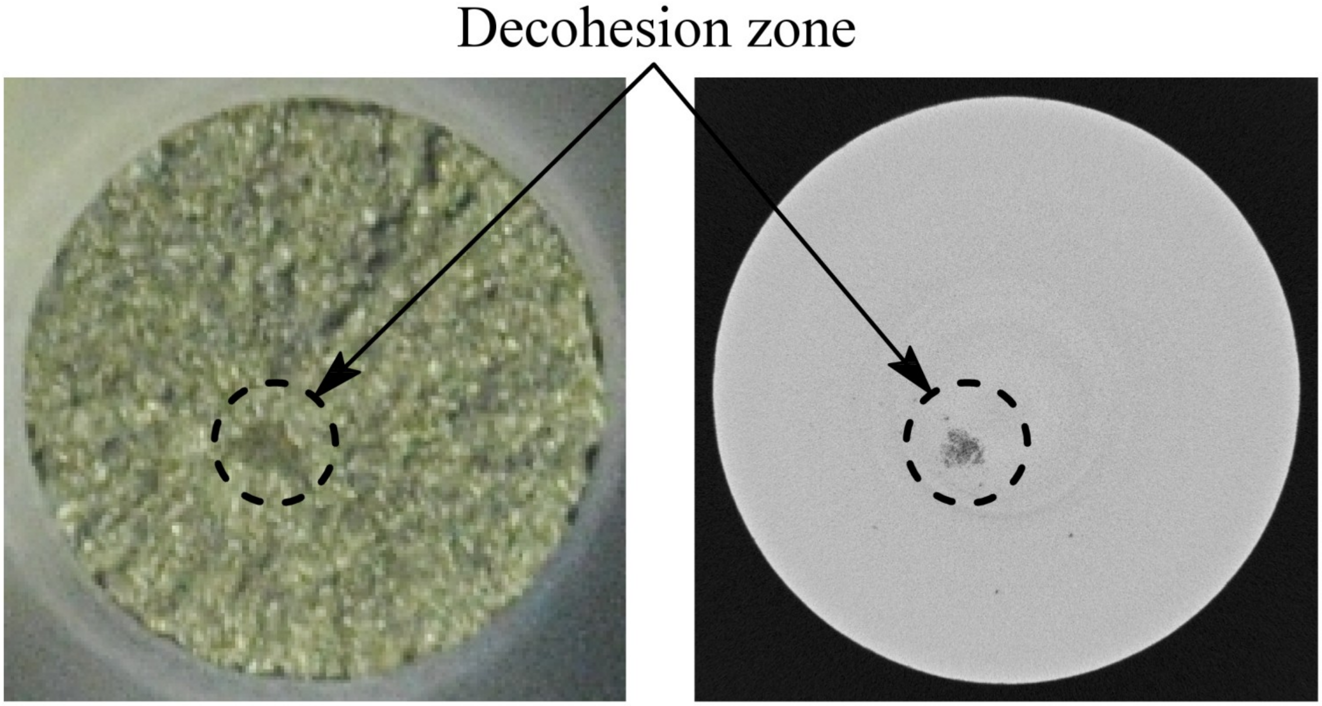

FIGURE 10

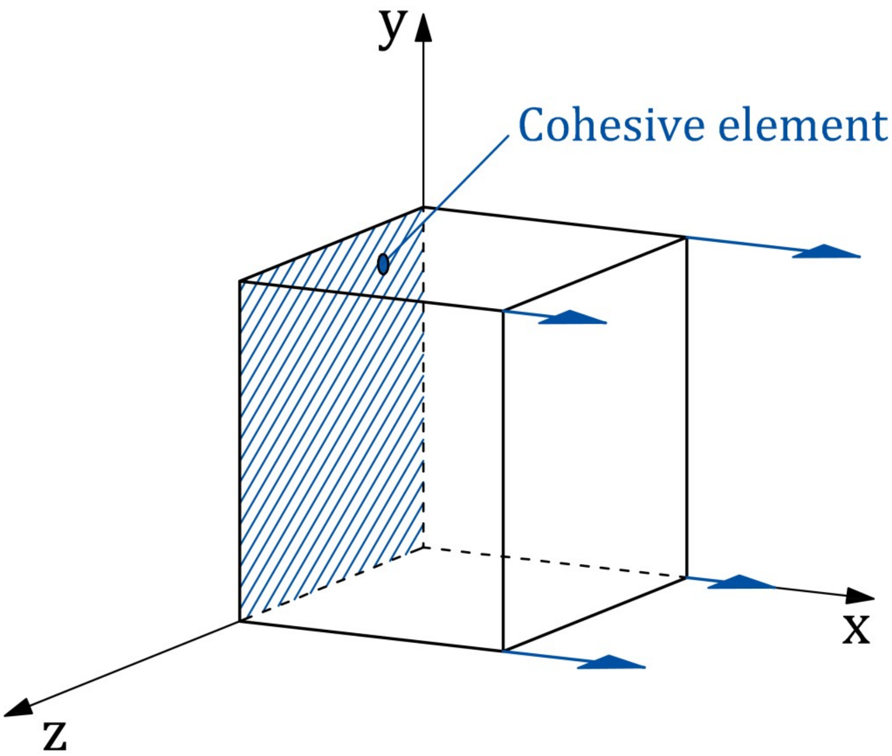

FIGURE 11

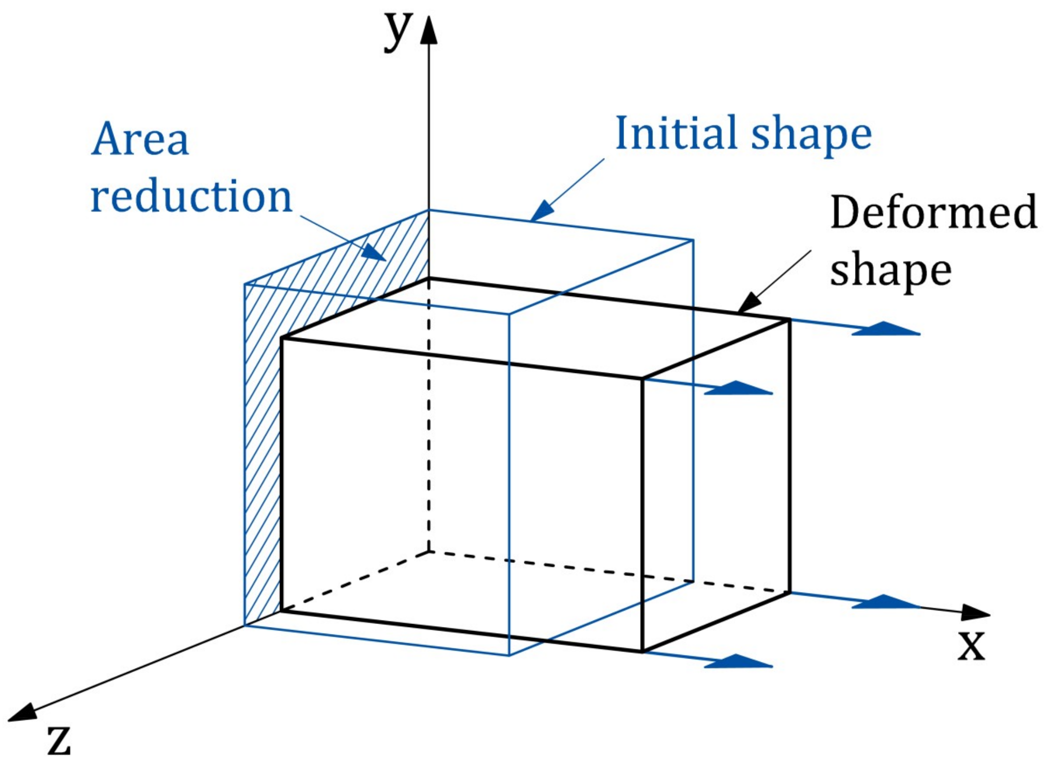

FIGURE 12

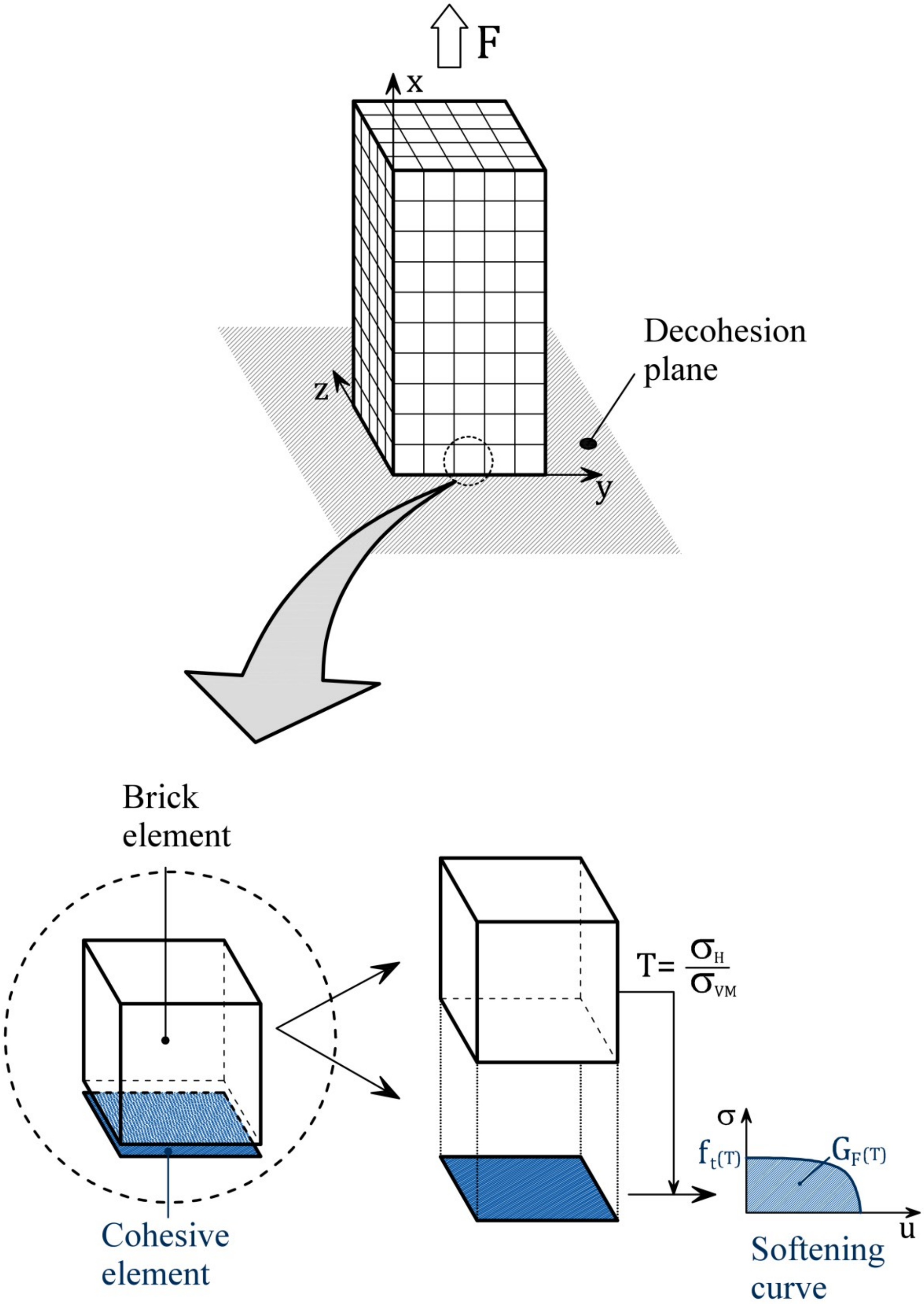
F
x
z
y
Decohesion plane
Brick element
Cohesive element
$T = \frac{\sigma_H}{\sigma_{VM}}$
σ
$f_{t(T)}$
$G_{F(T)}$
u
Softening curve

FIGURE 13

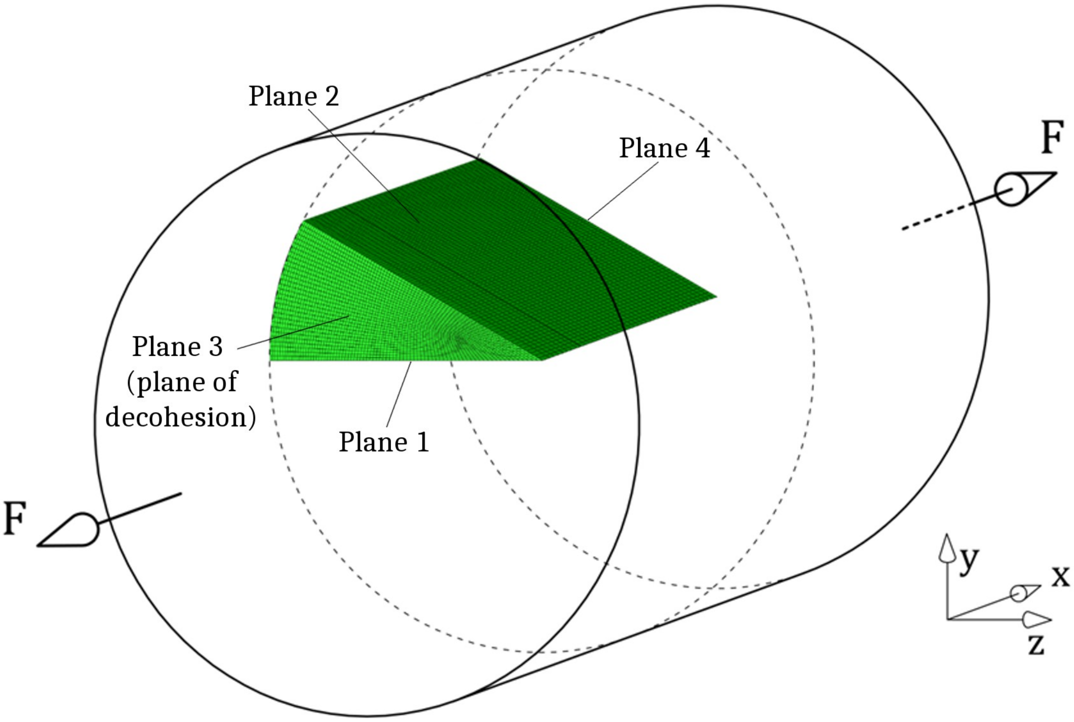

FIGURE 14

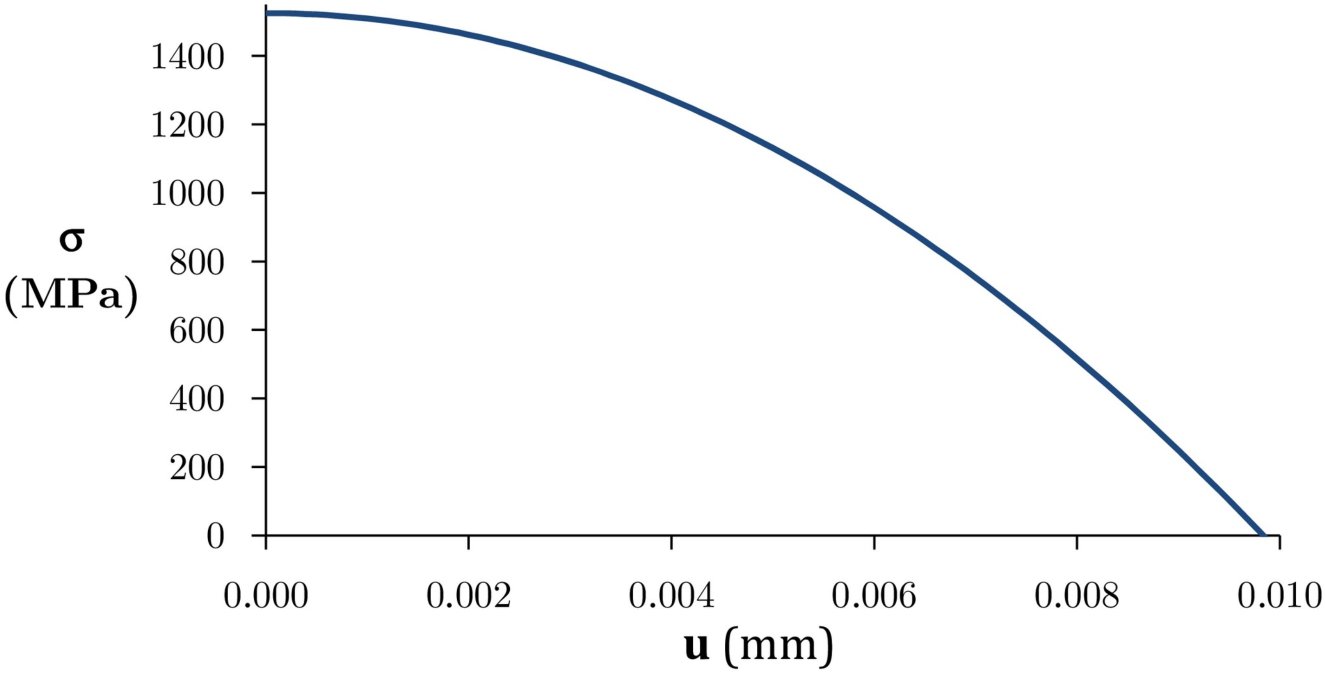
σ (MPa)
1400
1200
1000
800
600
400
200
0
0.000
0.002
0.004
0.006
0.008
0.010
u (mm)

FIGURE 15

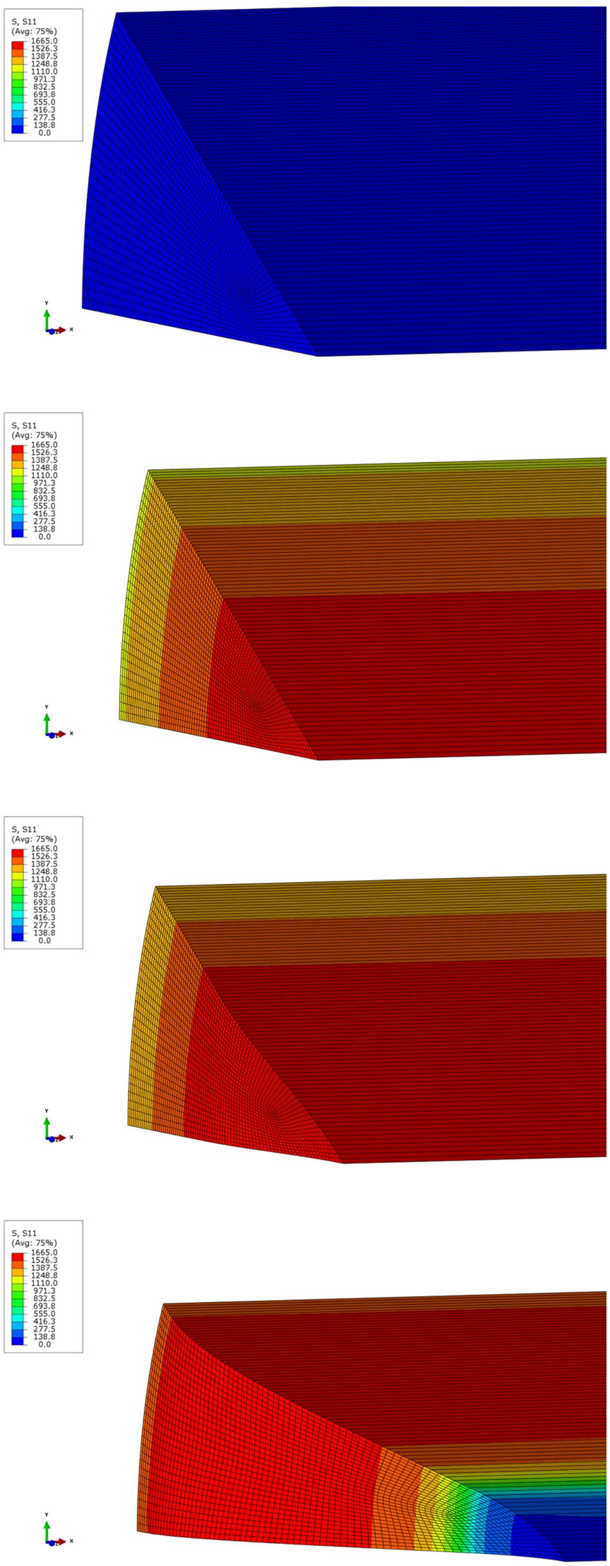
a)
b)
c)
d)

FIGURE 16

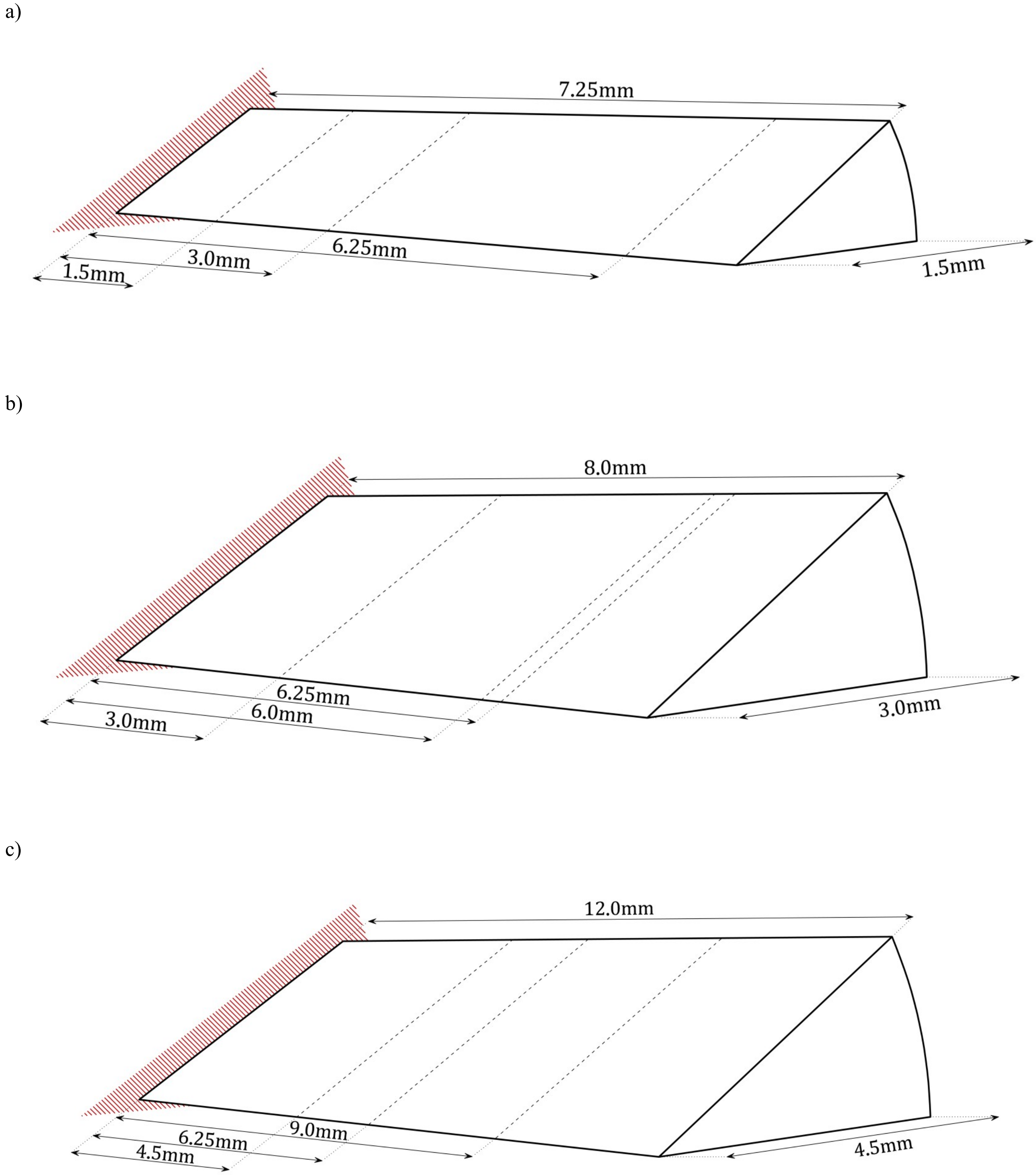
a)
7.25mm
6.25mm
3.0mm
1.5mm
1.5mm
b)
8.0mm
6.25mm
6.0mm
3.0mm
3.0mm
c)
12.0mm
9.0mm
6.25mm
4.5mm
4.5mm

FIGURE 17

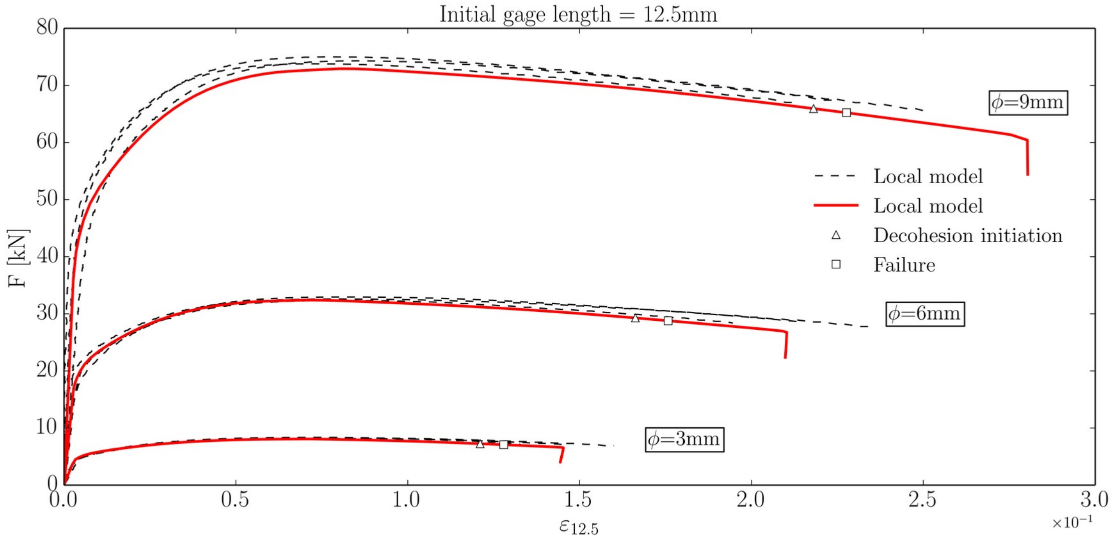
Initial gage length = 12.5mm
F [kN]
80
70
60
50
40
30
20
10
0
0.0
0.5
1.0
1.5
2.0
2.5
3.0
$\varepsilon_{12.5}$
$\times10^{-1}$
ϕ=9mm
ϕ=6mm
ϕ=3mm
Local model
Local model
Decohesion initiation
Failure

FIGURE 18

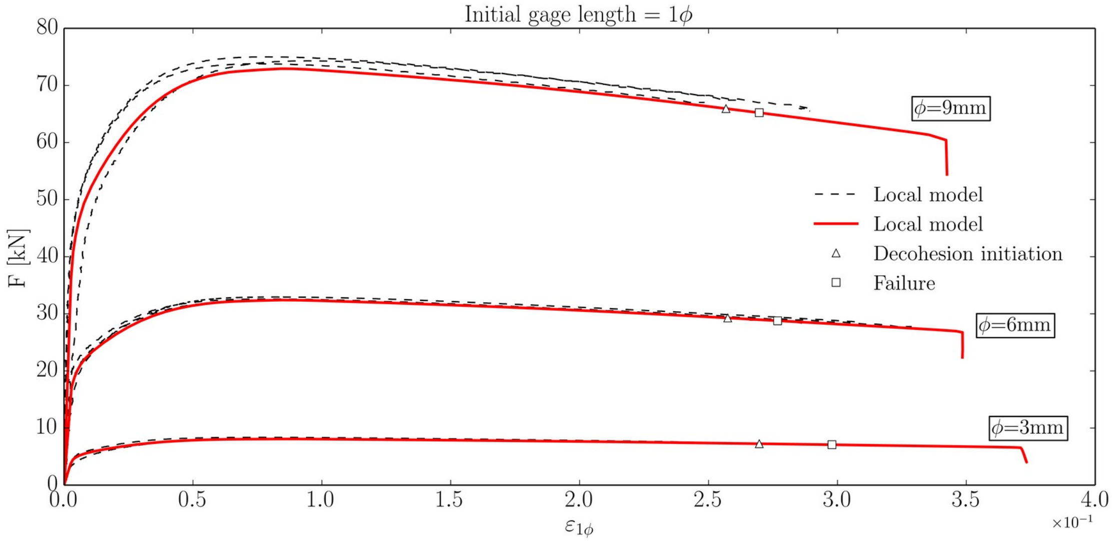
Initial gage length = 1ϕ
80
70
60
50
40
30
20
10
0
F [kN]
0.0
0.5
1.0
1.5
2.0
2.5
3.0
3.5
4.0
$\times 10^{-1}$
$\varepsilon_{1\phi}$
ϕ=9mm
ϕ=6mm
ϕ=3mm
Local model
Local model
Decohesion initiation
Failure

FIGURE 19

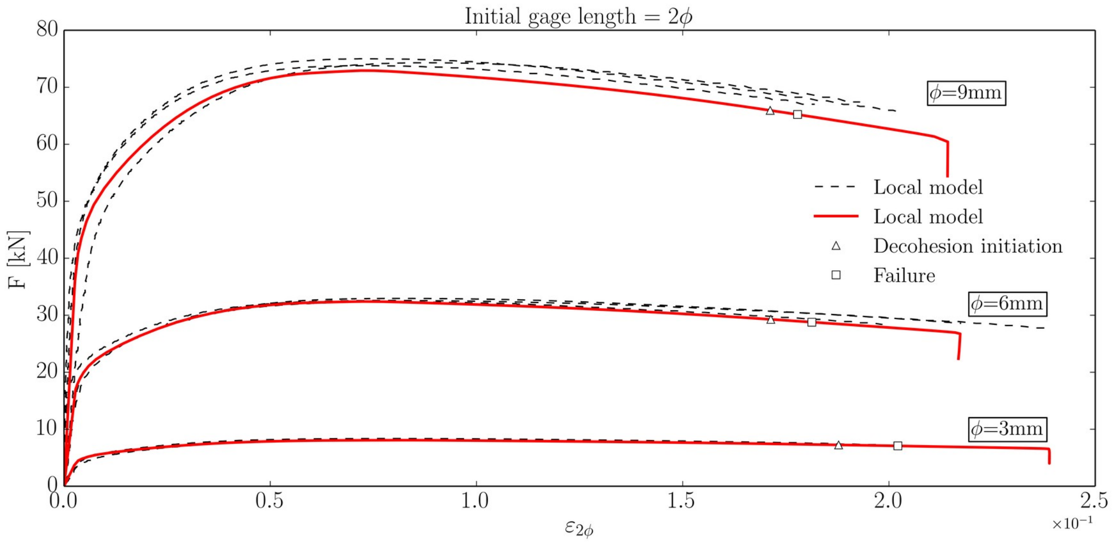
Initial gage length = 2ϕ
F [kN]
$\varepsilon_{2\phi}$
$\times 10^{-1}$
0
10
20
30
40
50
60
70
80
0.0
0.5
1.0
1.5
2.0
2.5
ϕ=9mm
ϕ=6mm
ϕ=3mm
Local model
Local model
Decohesion initiation
Failure

FIGURE 20

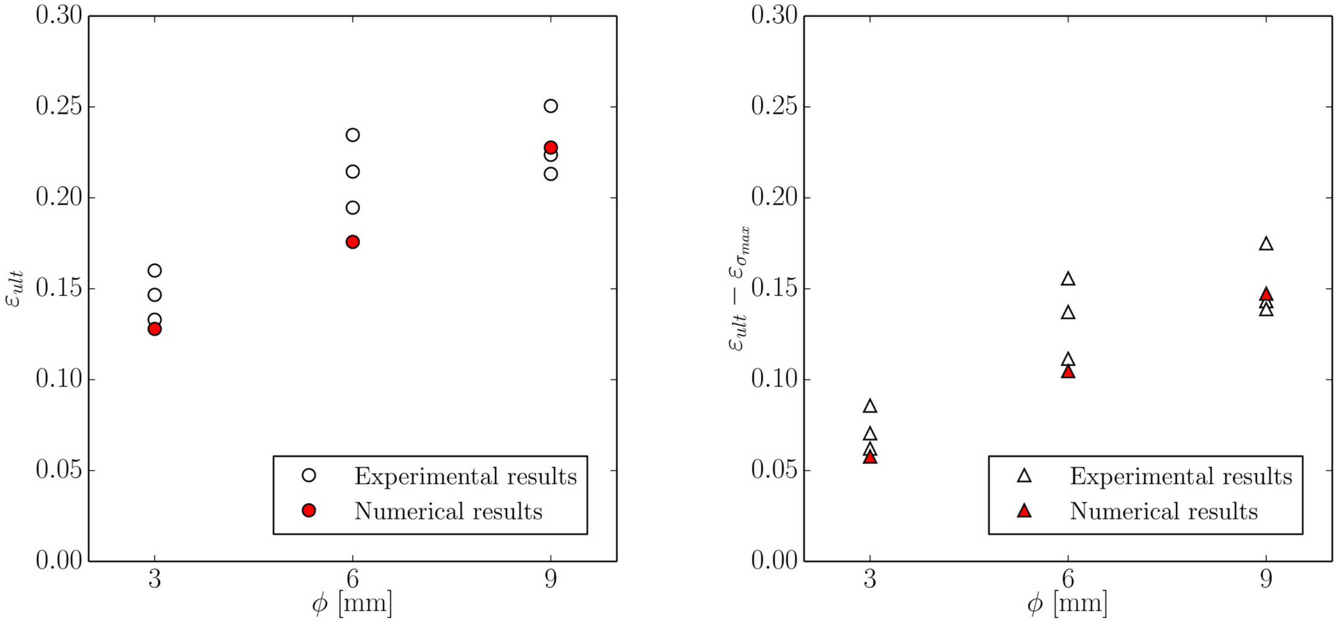
0.30
0.25
0.20
0.15
0.10
0.05
0.00
ε_{ult}
3
6
9
ϕ [mm]
○ Experimental results
● Numerical results
0.30
0.25
0.20
0.15
0.10
0.05
0.00
$\varepsilon_{ult} - \varepsilon_{\sigma_{max}}$
3
6
9
ϕ [mm]
△ Experimental results
▲ Numerical results

FIGURE 21

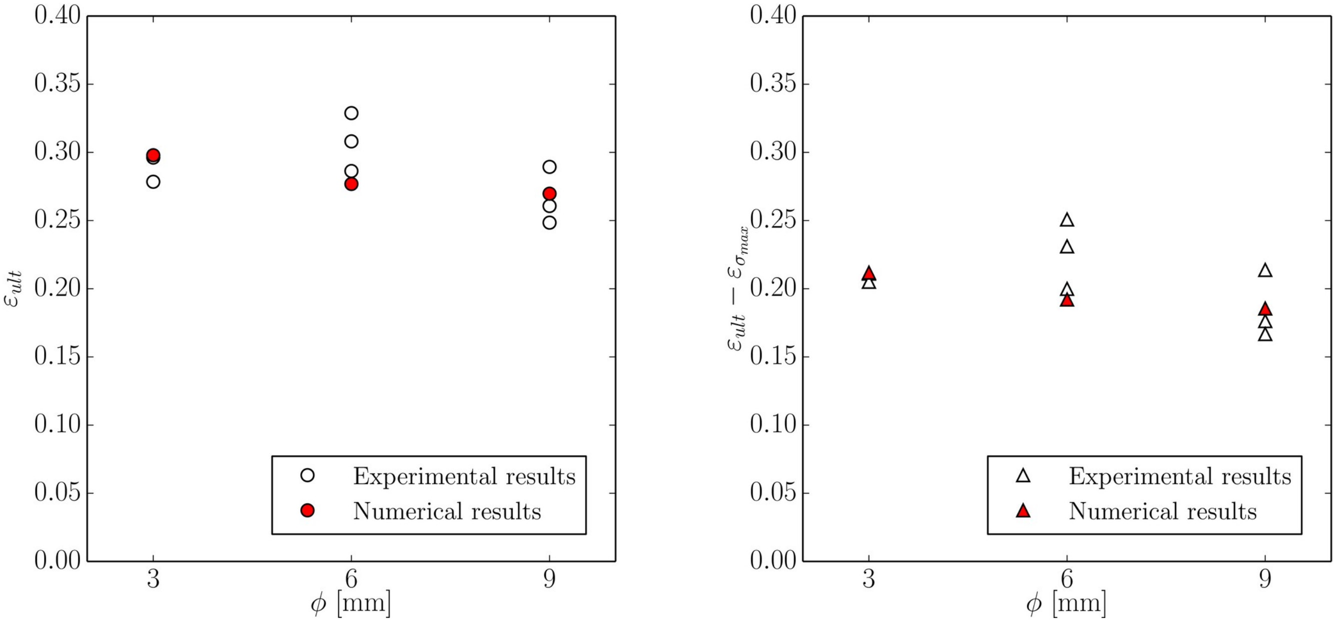
0.40
0.35
0.30
0.25
0.20
0.15
0.10
0.05
0.00
ε_{ult}
3
6
9
ϕ [mm]
Experimental results
Numerical results
0.40
0.35
0.30
0.25
0.20
0.15
0.10
0.05
0.00
$\varepsilon_{ult} - \varepsilon_{\sigma_{max}}$
3
6
9
ϕ [mm]
Experimental results
Numerical results

FIGURE 22

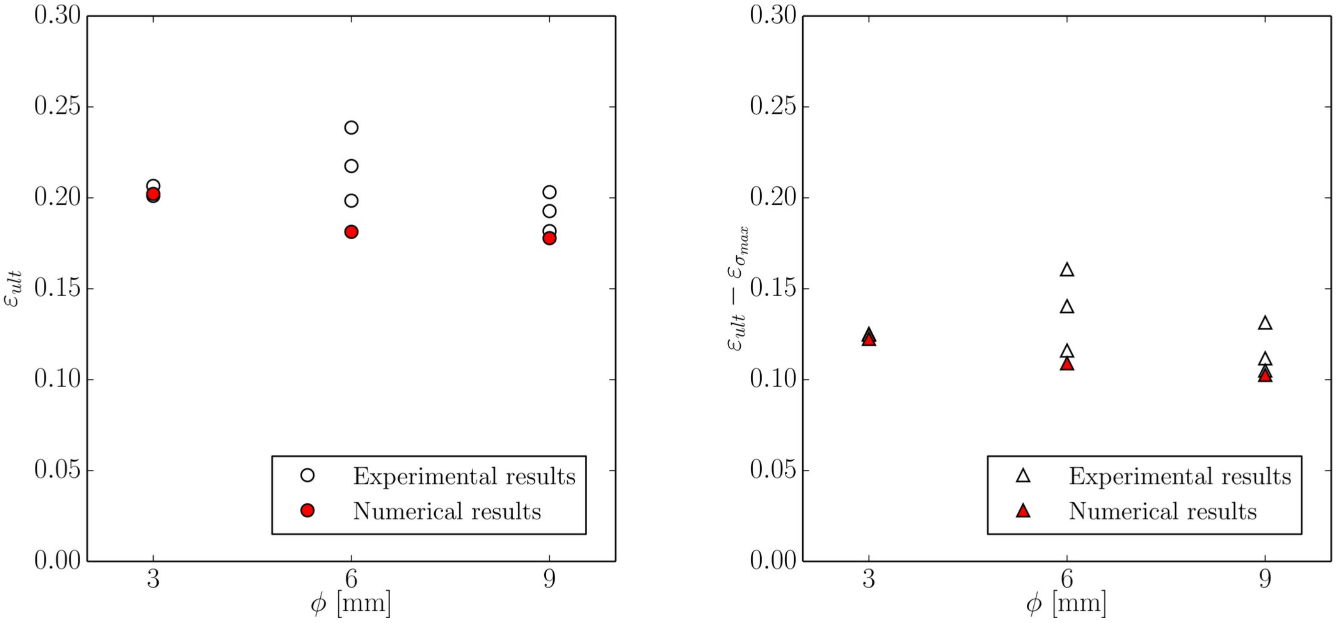

0.30
0.25
0.20
0.15
0.10
0.05
0.00
ε_{ult}
3
6
9
ϕ [mm]
○ Experimental results
● Numerical results
0.30
0.25
0.20
0.15
0.10
0.05
0.00
$\varepsilon_{ult} - \varepsilon_{\sigma_{max}}$
3
6
9
ϕ [mm]
△ Experimental results
▲ Numerical results

FIGURE 23